



TITLE:

Solidification depth and crystallization age of the Shiaidani Granodiorite: constraints to the average denudation rate of the Hida Range, central Japan

AUTHOR(S):

Kawakami, Tetsuo; Sueoka, Shigeru; Yokoyama, Tatsunori; Kagami, Saya; King, Georgina E.; Herman, Frédéric; Tsukamoto, Sumiko; Tagami, Takahiro

CITATION:

Kawakami, Tetsuo ...[et al]. Solidification depth and crystallization age of the Shiaidani Granodiorite: Constraints to the average denudation rate of the Hida Range, central Japan. *Island Arc* 2021, 30(1): e12414.

ISSUE DATE:

2021

URL:

<http://hdl.handle.net/2433/268306>

RIGHT:

This is the peer reviewed version of the following article:[Kawakami, T., Sueoka, S., Yokoyama, T., Kagami, S., King, G. E., Herman, F., Tsukamoto, S., & Tagami, T. (2021). Solidification depth and crystallization age of the Shiaidani Granodiorite: Constraints to the average denudation rate of the Hida Range, central Japan. *Island Arc*, 30(1), e12414.], which has been published in final form at <https://doi.org/10.1111/iar.12414>. This article may be used for non-commercial purposes in accordance with Wiley Terms and Conditions for Use of Self-Archived Versions. This article may not be enhanced, enriched or otherwise transformed into a derivative work, without express permission from Wiley or by statutory rights under applicable legislation. Copyright notices must not be removed, obscured or modified. The article must be linked to Wiley's version of record on Wiley Online Library and a...

1 **Solidification depth and crystallization age of the Shiaidani**
2 **Granodiorite: constraints to the average denudation rate of the Hida**
3 **Range, central Japan**

4

5 Tetsuo KAWAKAMI^{1, *}, Shigeru SUEOKA², Tatsunori YOKOYAMA², Saya6 KAGAMI², Georgina E. King³, Frédéric Herman³, Sumiko Tsukamoto⁴ and Takahiro7 TAGAMI¹

8

9 1: Department of Geology and Mineralogy, Graduate School of Science, Kyoto University,

10 Kitashirakawa-Oiwake-cho, Sakyo-ku, Kyoto 606-8502, Japan

11 2: Tono Geoscience Center, Japan Atomic Energy Agency, 959-31, Jorinji, Izumi-cho, Toki, Gifu, 509-

12 5102, Japan.

13 3: Institute of Earth Surface Dynamics, University of Lausanne, Lausanne, Switzerland

14 4: Leibniz Institute for Applied Geophysics, 30655 Hannover, Germany

15

16 * Corresponding author, t-kawakami@kueps.kyoto-u.ac.jp, ORCID ID: <https://orcid.org/0000->

17 0002-5921-5562

18

19 **Abstract**

20 Solidification pressure and crystallization age of the ca. 5 Ma Shiaidani Granodiorite (Hida Mountain
21 Range, central Japan) are determined based on Al-in-hornblende geobarometry and U-Pb zircon dating.
22 Al-poor patchy replacements developed in amphiboles are common in this granite and petrographic
23 study revealed that the replacements include chloritized biotite and albitic plagioclase. These are
24 probably the hydrothermally recrystallized domains, and should not be used for solidification pressure
25 estimates. Magmatic rim of amphibole is characterized by $Si < 7.3$ a.p.f.u. ($Al_{IV} > 0.7$ a.p.f.u.), and
26 utilized in solidification pressure estimate that yielded 0.17-0.29 GPa. The solidification age of the
27 granite is estimated as ca. 5.6-5.2 Ma using U-Pb zircon dating. From these data, the lower limit of an
28 average denudation rate after ca. 5.6-5.2 Ma for the area where Shiaidani Granodiorite is exposed is
29 estimated as 0.93-2.5 mm/yr.

30

31 **Keywords:** granite, exhumation, hornblende, patchy zoning

32

33 **1 Introduction**

34 Emplacement depth of granitoids in the upper continental crust in combination with their solidification
35 ages are useful in reconstructing the complex exhumation and tectonic processes of the region where
36 the granitoids are currently exposed. The Kurobe area, Hida Mountain Range, central Japan is

37 characterized by the exposure of the youngest granites in the world (Ito et al., 2013, 2017), and
38 exhumation history of the young granites have been of great interest (Yamada, 1997; Yamada &
39 Harayama, 1999; Spencer et al., 2019). However, results of low-temperature geochronological
40 methods are often thermally affected by the late-stage granite intrusions (Yamada & Harayama, 1999)
41 and a method to reliably constrain the depth and age information was needed.

42 The Al-in-hornblende barometer (Anderson & Smith, 1995; Hammarstrom & Zen, 1986;
43 Mutch et al., 2016; Schmidt, 1992) has long been used to constrain the solidification pressure of
44 granitoid plutons. In applying the Al-in-hornblende barometer, choosing a right composition of
45 hornblende is very important, because the barometer uses the Al content of amphibole that crystallized
46 at the granite solidus. Mutch et al. (2016) recommended to use amphibole analyses taken from the
47 rims of grains, in contact with plagioclase and in apparent textural equilibrium with the rest of the
48 mineral assemblage at temperatures close to the haplogranite solidus, as determined from amphibole–
49 plagioclase thermometry. However, using the rim composition of amphibole is not a successful
50 criterion in the case of hornblende with patchy Al zoning (e.g., Yamaguchi et al., 2003; Hartung et al.,
51 2017), which is probably a result of post-magmatic hydrothermal alteration. As a criterion of
52 amphibole crystallized under magmatic or subsolidus conditions, Chivas (1981) proposed that
53 amphiboles with $Si > 7.3$ a.p.f.u. for $O = 23$ ($Al_{IV} < 0.7$ a.p.f.u.) are not truly magmatic and crystallized
54 under subsolidus conditions in the presence of a fluid phase. On the other hand, in the study of the

55 Takidani Pluton (Hida Range), [Hartung et al. \(2017\)](#) considered low-Al and high-Al amphiboles
56 observed as patchy zones could have formed under near-isobaric conditions and difference in Al may
57 be related to the temperature and chemical variability of the melt from which they crystallized
58 ([Hartung et al., 2017](#)). Therefore, careful microstructural observation on the coexisting minerals of
59 each amphibole domain is required to understand the development of patchy zones in amphibole, and
60 to finally constrain the solidification pressure of the pluton.

61 This study examines mode of occurrence and chemical composition of amphibole in the
62 Shiaidani Granodiorite in detail to constrain the formation timing of the patchy domains. We
63 petrographically constrain suitable amphibole domains/compositions that coexisted with the necessary
64 phases to apply the Al-in-hornblende barometry (e.g., [Mutch et al., 2016](#)) and estimate the
65 solidification pressure of the Shiaidani Granodiorite. In combination with the U-Pb zircon dating of
66 the granodiorite, average denudation rate after ca. 5.6-5.2 Ma is finally constrained for the area where
67 Shiaidani Granodiorite is exposed. In this study, we follow the definition of “exhumation” and
68 “denudation” by [Ring et al. \(1999\)](#), [Reiners and Brandon \(2006\)](#) and [Sueoka and Tagami \(2019\)](#).
69 “Exhumation” is the vertical distance traveled by rocks relative to Earth’s surface and “denudation”
70 takes into account the lateral movement of the exhumed rocks.

71

72 **2 Geological setting**

73 The Shiaidani Granodiorite crops out in the Kurobe area, Hida Mountain Range, central Japan (Figure
74 1). It is exposed as elongate-shaped pluton with a NS length of ~12 km and maximum EW width of
75 ~3 km (Harayama, 2015). The world's youngest granite, the Kurobegawa Granite (ca. 0.8 Ma), is
76 exposed along the Kurobegawa River (Ito et al., 2013; 2017; Spencer et al., 2019). It is accompanied
77 by young volcanics such as 1.7-1.6 Ma Jiigatake Volcanics (mainly rhyolitic welded tuff and andesite
78 and rhyolite lavas) and 1.6 Ma Shirakawa-tengu Volcanics (mainly rhyolitic welded tuff) to the east
79 (Figure 1; Harayama et al., 2015). The Kurobegawa Granite intrudes the Jiigatake Volcanics
80 (Harayama et al., 2010). The Shiaidani Granodiorite is exposed roughly to the west of Kurobegawa
81 River. It was previously considered as a part of the Kurobe-bessan Granite (Harayama et al., 2010),
82 which was divided into the Shiaidani Granodiorite (ca. 5.5-5.4 Ma) and the Kuranosuke Granite (ca.
83 9.5-9.1 Ma) based on the difference in U-Pb zircon ages (Harayama, 2015; Ito et al., 2013). The
84 Kuranosuke Granite is distributed to the west of the Shiaidani Granodiorite (Figure 1). The Shiaidani
85 Granodiorite is also dated to be ca. 7.1-5.1 Ma and ca. 5.1-4.3 Ma by K-Ar dating of hornblende and
86 biotite, respectively (Ogata et al., 1983; Yamada & Harayama, 1999; Harayama, 2015; Harayama et
87 al., 2010). The zircon fission track age is dated at ca. 1.5 Ma (Harayama et al., 2010). The Kuranosuke
88 Granite, on the other hand, is dated at ca. 5.1 Ma by K-Ar dating of biotite (Harayama et al., 2010).
89 Based on the existence of a decussate structure of biotite, Harayama et al. (2010) considered that
90 recrystallization due to thermal metamorphism was evident in the Kurobe-bessan Granite.

91

92 **3 Analytical methods**

93 Quantitative analyses of rock-forming minerals and X-ray elemental mapping of thin section samples

94 were performed by a JEOL JXA-8105 superprobe at Kyoto University. Analytical conditions for

95 quantitative analyses were 15.0 kV acceleration voltage, 10 nA beam current, and 3 μm beam diameter.

96 The counting time for the peak and backgrounds were 30 s and 15 s for Cl, 60 s and 30 s for F, and 10

97 s and 5 s for other elements. Natural and synthetic minerals were used as standards and the ZAF

98 correction was applied. Representative mineral analyses are given in [Table 1](#). Recalculation of ferric99 iron in amphibole and calculation of amphibole formula are based on [Holland and Blundy \(1994\)](#).

100 Two granite samples were crushed in a rod mill and stainless steel mortar. Zircon grains

101 were separated by panning, magnetic separation and using heavy liquid at Kyoto Fission-Track Co.

102 Ltd. After handpicking under a stereomicroscope, zircon grains were mounted in epoxy resin (Struers

103 Specifix-20). Cathodoluminescence (CL) images of zircon grains were obtained by using a field

104 emission electron microprobe JEOL JXA-8530F at Japan Atomic Energy Agency, Tono Geoscience

105 Center (JAEA, TGC). Analysis points were selected to avoid cracks and inclusions using CL images.

106 U-Pb isotopic analysis by laser ablation-inductively coupled plasma-mass spectrometry

107 (LA-ICP-MS) was performed in JAEA, TGC using Thermo Fisher Scientific Neptune-Plus coupled

108 with Photon-Machines Analyte G2 Excimer laser on separate zircon grains. For U-Pb isotope analysis

109 to estimate the zircon crystallization ages, the 91500 zircon (Wiedenbeck et al., 1995, 2004) was used
 110 as the primary reference and standard material to correct the mass bias effect on $^{206}\text{Pb}/^{238}\text{U}$ and
 111 $^{207}\text{Pb}/^{206}\text{Pb}$, respectively. Duplicate measurements of the secondary reference materials of OD-3 (33.0
 112 ± 0.1 Ma: Iwano et al., 2013) were carried out to assess the age data obtained from the unknown
 113 samples. Details of the analytical conditions are given in Table S1. Isoplot 4.15 (Ludwig, 2012) was
 114 used to create concordia diagrams and calculation of a weighted mean age.

115 In order to obtain accurate crystallization ages for young (<2 Ma) zircon, it is necessary to
 116 consider the contributions of common Pb and initial disequilibrium caused by Th/U and Pa/U
 117 fractionation in the zircon-melt system (Sakata et al., 2017; Sakata, 2018). We performed the
 118 correction for common Pb by a single correction based on a modified Tera-Wasserburg concordia
 119 diagram (modified ^{207}Pb method; Sakata, 2018). In order to confirm the initial disequilibrium on the
 120 zircon data obtained in this study, we also made correction of the initial disequilibrium effect and
 121 compared it with the equilibrium results. For the initial disequilibrium correction, we used the average
 122 Th/U ratio of analyzed zircon (0.67) for the Th/U ratio of zircon grains at the time of zircon
 123 crystallization $[(\text{Th}/\text{U})_{\text{Zircon}}]$. Th/U ratio of the melt $[(\text{Th}/\text{U})_{\text{Melt}}]$ was assumed to be 4.8, which was an
 124 average derived from river sand samples collected in the vicinity of the Kurobegawa Granite (Imai et
 125 al., 2004; Ito et al., 2013). Then, we used a Th/U fractionation factor $[f_{\text{Th}/\text{U}} = (\text{Th}/\text{U})_{\text{Zircon}}/(\text{Th}/\text{U})_{\text{Melt}}]$
 126 of 0.123 with 30% of estimation error for the initial Th/U fractionation correction. In this study, we

127 assumingly used general value of Pa/U fractionation factor between melt and zircon [$f_{\text{Pa/U}} =$
 128 $(\text{Pa/U})_{\text{Zircon}}/(\text{Pa/U})_{\text{Melt}}$] of 3.36 with 30% of estimation error (compilation value based on Rioux et al.,
 129 2015; Sakata et al., 2017; Schmitt, 2011), because we did not determine a Pa/U partitioning factor.)

130

131 **4 Sample description**

132 Two unweathered samples of the Shaidani Granodiorite (Harayama, 2015) were collected from the
 133 outcrop exposures (Figure 1). These samples are likely affected by post-magmatic hydrothermal
 134 activity as indicated by complex patchy chemical zoning of amphibole, chloritization of biotite and
 135 partial sericitization of plagioclase. In order to check coexistence of mineral phases required for the
 136 application of the Al-in-hornblende geobarometry, a detailed mineral description is made for these
 137 samples.

138 Sample KRG16-07 is a hornblende-biotite granite (Figure 2), which was collected at the
 139 same outcrop as KRG-07 showing U-Pb zircon age of 5.6 ± 0.1 Ma (Ito et al., 2013). Matrix mineral
 140 assemblage of this sample is amphibole + biotite (mostly chloritized) + plagioclase + quartz + K-
 141 feldspar + magnetite + titanite + zircon + apatite + allanite. Amphibole shows gradual core/rim
 142 chemical zoning accompanied by discontinuous patchy replacements; the core and patchy
 143 replacements are dark under the back scattered electron (BSE) images whereas the rim is slightly
 144 bright under the BSE images (Figure 2c). The core is weakly enriched in Mg (Figure 2f) and Na

145 (Figure 2h), while the rim is weakly enriched in Fe (Figure 2d) and K (Figure 2k). The patchy
 146 replacements are enriched in Mg (Figure 2f), Mn and Si, and depleted in Fe (Figure 2d), Al (Figure
 147 2e), Cl (Figure 2g), Na (Figure 2h) and K (Figure 2k) compared to the core. The amphibole is mostly
 148 magnesiohornblende except for the final-stage rim and patches corresponding to actinolite (Figure 3).
 149 The amphibole core and rim enclose biotite, K-feldspar, plagioclase, ilmenite, magnetite, zircon and
 150 apatite. On the other hand, the patchy replacements include biotite (partly chloritized), plagioclase,
 151 titanite, K-feldspar, magnetite, zircon and apatite. Oscillatory-zoned plagioclase shows a decrease in
 152 anorthite content at the rim, and the plagioclase rim in contact with hornblende rim shows composition
 153 of An₁₄₋₂₂. An albitic outermost rim (<An₁₄) is locally developed on the An₁₄₋₂₂ plagioclase, and
 154 such plagioclase is commonly in contact with patchy replacements. The composition of albitic
 155 plagioclase enclosed in the patchy replacements is similar to the composition of the outermost albitic
 156 rim of matrix plagioclase (Figure 2e, i).

157 Sample KRG16-101 is a hornblende-biotite granite (Figure 4). Matrix mineral assemblage
 158 is amphibole + biotite + plagioclase + quartz + K-feldspar + magnetite + titanite + zircon + apatite +
 159 allanite. Chloritization of biotite is weaker compared to sample KRG 16-07, and is only limited to the
 160 rims and along the cleavages of biotite. Amphibole shows core/rim chemical zoning with patchy
 161 zoning under BSE images. The gradual core/rim zoning is recognized as darker core with brighter rim
 162 under the BSE images (Figure 4c). The discontinuous, commonly BSE-dark patchy replacements cut

163 the gradual zoning pattern. The rim is enriched in Fe (Figure 4e), Na (Figure 4i), K (Figure 4l) and
 164 Mn, and depleted in Mg (Figure 4g) compared to the core. The BSE-dark patchy replacements are
 165 more depleted in Mg (Figure 4g), Al (Figure 4f), Cl (Figure 4h) and Na (Figure 4i), and enriched in Si
 166 (Figure 4d) and Mn as observed by X-ray chemical mappings. The amphibole is mostly
 167 magnesiohornblende except for the final-stage patchy replacements that correspond to actinolite
 168 (Figure 5). The amphibole core and rim include plagioclase (rim with An18), K-feldspar, quartz,
 169 magnetite, ilmenite, apatite, zircon whereas the patchy replacements include albitic plagioclase, K-
 170 feldspar, quartz, chloritized biotite, magnetite, titanite, apatite, zircon. Composite pseudo-inclusion of
 171 K-feldspar and albitic plagioclase, which is connected with matrix via cracks, is commonly developed
 172 even in the core of amphibole. Oscillatory-zoned plagioclase in the matrix shows decrease in anorthite
 173 content at the rim, and the composition of the rim in contact with amphibole rim is An14-26. Locally,
 174 albitic film (<An14) is developed at the plagioclase rim. On the other hand, amphibole is enclosed in
 175 plagioclase showing various compositions of An39-52, An39-41 (core) and An16-17 (rim).

176

177 **5 U-Pb zircon dating of KRG16-101**

178 Zircons in this sample is commonly euhedral, and present in the matrix and also enclosed in biotite,
 179 hornblende, quartz and K-feldspar. It is oscillatory- and sector-zoned under CL images (Figure 6, inset).
 180 Mineral inclusions such as apatite are common in zircon. Th/U ratio of oscillatory-zoned rim ranges

181 from 0.42 to 1.08 (0.65 in average). Dates of oscillatory-zoned rims are determined for sample
 182 KRG16-101, and the results are summarized in [Table S2](#). Concordia plots with 1σ error ellipses show
 183 that the analytical results not corrected for the contribution of the common Pb and initial disequilibria
 184 are discordant ([Figure 6](#)). Common Pb-corrected weighted average of the 24 analysis spots yielded
 185 ^{238}U - ^{206}Pb age of 5.20 ± 0.17 Ma (95% confidence level, MSWD = 0.27, probability = 0.999). The
 186 initial disequilibrium correction resulted in ~2% difference in the weighted average age, *i.e.*, 5.31
 187 ± 0.17 Ma (95% confidence level, MSWD = 0.27, probability = 1.000). For simplicity, we prefer the
 188 former age assuming initial equilibrium in this study.

189

190 **6 Amphibole composition and application of Al-in-hornblende geobarometry**

191 The chemical composition of amphiboles in sample KRG 16-07 is plotted in [Figure 3](#) and that in
 192 sample KRG16-101 is plotted in [Figure 5](#). As described above, amphibole represents gradual chemical
 193 zoning from the core to the rim, and discontinuous patchy replacements cut this texture ([Figures 3 and](#)
 194 [5](#)). In creating [Figures 3 and 5](#), the cores, rims and replacements are classified based mainly on BSE
 195 images and partly on X-ray mappings. Therefore, discrimination between gradual core and rim was
 196 not always easy under the BSE images alone, and caused scattering of core points within rim-dominant
 197 compositional areas ($\text{Si} > \sim 7.1$ a.p.f.u. and $\text{Al}_{\text{IV}} < \sim 0.9$ a.p.f.u. areas of [Figures 3 and 5](#)). Nevertheless,
 198 it is important that original core/rim zoning and discontinuous patchy replacements are chemically

199 discriminated at around $Si = 7.3$ a.p.f.u. and $Al_{IV} = 0.7$ a.p.f.u. ($O = 23$) for both samples (Figures 3
 200 and 5).

201 Because patchy replacements include secondary minerals such as albitic plagioclase,
 202 chloritized biotite, and composite pseudo-inclusion of K-feldspar and albitic plagioclase that is
 203 connected with matrix via cracks (Figures 2 and 4; note inclusion minerals in Al-poor patches), it is
 204 considered that the patchy replacements are the recrystallized domains during hydrothermal alteration.
 205 The most extensive amphibole composition that patchy replacements show is actinolitic composition
 206 (Figures 3 and 5), and coexistence of such domains with albitic plagioclase and chloritized biotite also
 207 supports the alteration under subsolidus hydrothermal condition.

208 On the other hand, amphibole domains that show original core/rim zoning preserve
 209 amphibole composition of igneous stage as supported by presence of more calcic plagioclase
 210 inclusions (~An18) as well as higher Al contents of the amphibole domains compared to the
 211 replacements. The mineral inclusions in the igneous amphibole domains (plagioclase, K-feldspar,
 212 quartz, magnetite, ilmenite, apatite) and the matrix minerals in contact with amphibole rim (biotite,
 213 plagioclase rim) satisfy the mineral assemblage required for the application of Al-in-hornblende
 214 geobarometer (Mutch et al., 2016). Therefore, Al-in-hornblende geobarometer is applied to the
 215 amphibole rim to constrain the solidification pressure of the granite. Hornblende-plagioclase
 216 geothermometer (Holland & Blundy, 1994) is also applied to the amphibole rim and plagioclase rim

217 in contact with the amphibole rim. Composition of amphibole rim enclosed in plagioclase rim is also
 218 used for the *P-T* estimate (Figure 7). Although *P-T* estimates from patchy replacement is not
 219 considered to represent the solidification condition, they are also plotted in Figure 7 for comparison.
 220 The Mutch et al. (2016) calibration is preferred in this study, because it is experimentally calibrated
 221 for pressure down to 0.8 kbar and applicable to shallower plutons without extrapolation compared to
 222 previous calibrations (e.g., 2.5-13 kbar for Schmidt, 1992). Additionally, calibration dataset of Mutch
 223 et al. (2016) involves very wide range of plagioclase composition (An15-76), and applicable without
 224 extrapolation to the mineral assemblage with low-An plagioclase (\geq An15) as in the case of the studied
 225 samples.

226 Application of the Al-in-hornblende geobarometer (Mutch et al., 2016) and hornblende-
 227 plagioclase geothermometer (Holland & Blundy, 1994) to the amphibole rim and plagioclase rim pair
 228 resulted in 616-691°C and 0.17-0.27 GPa (\pm 0.04 GPa) for KRG 16-07, and 620-702°C and 0.17-0.29
 229 GPa (\pm 0.05 GPa) for KRG16-101 (Figure 7). These *P-T* estimates are plotted on the haplogranite
 230 solidus within error (Figure 7). Assuming rock density of 2700 kg/m³ and lithostatic pressure gives
 231 solidification depths of 6.3 \pm 1.0 km to 10.3 \pm 1.7 km for KRG 16-07, and 6.4 \pm 1.0 km to 11.0 \pm 1.8 km
 232 for KRG 16-101.

233

234 **7 Discussion**

235 **7.1 Discriminating magmatic and hydrothermally recrystallized amphibole**

236 The Kurobe area exposes younger granite of ca. 0.8 Ma (Ito et al., 2013; 2017; Spencer et al., 2019),
 237 and estimation of denudation rate by low-temperature geochronology can be thermally affected by
 238 younger intrusions. On the other hand, estimation of exhumation rate based on Al-in-hornblende
 239 geobarometry is not strongly affected by later intrusions if the post crystallization, hydrothermal
 240 recrystallization of amphibole can be properly evaluated. The exhumation rate can be considered as
 241 the lowest estimate of an average denudation rate of the area, because denudation takes into account
 242 the lateral movement of the exhumed rocks (Batt & Braun, 1999; Ring et al., 1999; Reiners & Brandon,
 243 2006; Sueoka & Tagami, 2019).

244 Chivas (1981) proposed that amphiboles with $Si > 7.3$ a.p.f.u. ($Al_{IV} < 0.7$ a.p.f.u.) are not
 245 truly magmatic and crystallized under subsolidus conditions in the presence of a fluid phase. In this
 246 study, chemical boundary between rim and discontinuous patchy replacements of amphibole,
 247 determined based on microtextural observation, is recognized at $Si = 7.3$ a.p.f.u. and $Al_{IV} = 0.7$ a.p.f.u.
 248 (Figures 3 and 5). The patchy replacements commonly enclose and coexist with albitic plagioclase
 249 and chloritized biotite, which is consistent with the interpretation of Chivas (1981) that it is the
 250 recrystallized domain under subsolidus conditions in the presence of a fluid phase. Some of the P - T
 251 conditions estimated using the patchy replacements and the plagioclase composition in contact with
 252 them are plotted away from the haplogranite solidus (Figure 7), supporting the subsolidus origin of

253 patchy replacements. Therefore, criterion of [Chivas \(1981\)](#) is applicable to the Shiaidani Granodiorite
254 as well, and patchy replacements should not be used in estimating the solidification pressure of the
255 granite, although some of the patches yield pressure similar to that obtained from the magmatic
256 amphibole rim ([Figure 7](#)).

257

258 **7.2 Estimating the lower limit of the average denudation rate of the Shiaidani Granodiorite area** 259 **after ca. 5.6-5.2 Ma**

260 The presence of magmatic oscillatory zoning and absence of secondary replacement microtextures in
261 the dated zircon grains ([Figure 6a inset](#)) suggests that the U-Pb zircon ages of ca. 5.6-5.2 Ma can be
262 interpreted as the crystallization ages of these samples. By dividing the estimated solidification depths
263 by the U-Pb zircon age, average exhumation rate of the Shiaidani Granodiorite is estimated as 0.93-
264 2.2 mm/yr from KRG 16-07 and 1.0-2.5 mm/yr from KRG 16-101. This is considered to be the lowest
265 estimate of the average denudation rate since ca. 5.6-5.2 Ma for the area where the Shiaidani
266 Granodiorite is exposed. Nonetheless, uplift and denudation in the northern Hida Range, including the
267 Kurobe area, could be accelerated since ca. 1.5-1.0 Ma, considering depositional ages of granitic
268 gravels sourced from the Hida Range to the Matsumoto basin to the east ([Oikawa & Wada, 2004](#)). The
269 estimation in this study may provide the lower limit of the denudation rates since ca. 1.5-1.0 Ma,
270 considering the higher denudation rates (several to 10 mm/yr at a maximum) in shorter timescales

271 estimated based on the sedimentary yields in catchments (Ohmori, 1978; Fujiwara et al., 1999) and
272 terrestrial *in-situ* cosmogenic nuclide techniques (Matsushi et al., 2014).

273

274 **8 Conclusion**

275 We estimated the solidification depth of the Shiaidani Granodiorite utilizing Al-in-hornblende
276 geobarometry and solidification age using U-Pb zircon dating. The Al-poor patchy replacements
277 developed in amphiboles are probably hydrothermally recrystallized domains and should not be used
278 for solidification pressure estimates. The lower limit of an average denudation rate after ca. 5.6-5.2
279 Ma for the area where Shiaidani Granodiorite is exposed is estimated as 0.93-2.5 mm/yr.

280

281 **Acknowledgement**

282 We would like to thank Dr. Hisatoshi Ito and an anonymous reviewer for constructive comments, and
283 Prof. Tomokazu Hokada and Prof. Tatsuki Tsujimori for editorial efforts. This study was funded by
284 the Ministry of Economy, Trade and Industry (METI), Japan as part of its R&D supporting program
285 titled “Establishment of Advanced Technology for Evaluating the Long-term Geosphere Stability on
286 Geological Disposal Project of Radioactive Waste (Fiscal Years 2018 and 2020)”. This work was also
287 supported by the Grant-in-Aid for Scientific Research on Innovative Areas (KAKENHI No.
288 26109003) from the Ministry of Education, Culture, Sports, Science and Technology (MEXT). The

289 mineral separation was performed by Dr. Tohru Danhara and Dr. Hideki Iwano (Kyoto Fission-Track
290 Co., Ltd.). The field survey was supported by Dr. Tetsuya Komatsu, Shuji Terusawa (JAEA), Shoma
291 Fukuda, Takayuki Arai (Kyoto University), Yasuhisa Hino (KANSO Co., Ltd.), and staffs of the
292 Azohara Onsen Goya, Senninike Hutte, and Kansai Electric Power Co., Inc. TK thanks Kota Suzuki
293 and Ayu Yamazaki (Kyoto University) for discussion. GEK acknowledges financial support for
294 sample collection from a Mobility Grant from the University of Cologne and Swiss National
295 Science Foundation (SNSF) grant number PZ00P2_167960.

296

297 **ORCID IDs**298 Tetsuo Kawakami, <https://orcid.org/0000-0002-5921-5562>299 Shigeru Sueoka, <https://orcid.org/0000-0002-5264-2713>300 Tatsunori Yokoyama, <https://orcid.org/0000-0003-0667-6207>301 Saya Kagami, <https://orcid.org/0000-0001-5704-079X>302 Georgina E. King, <https://orcid.org/0000-0003-1059-8192>303 Frédéric Herman, <https://orcid.org/0000-0002-7237-4656>304 Sumiko Tsukamoto, <https://orcid.org/0000-0003-4626-4784>305 Takahiro Tagami, <https://orcid.org/0000-0002-4209-5541>

306

307 **References**

- 308 Anderson, J.L., & Smith, D.R. (1995). The effects of temperature and fO_2 on the Al-in-hornblende
309 barometer. *American Mineralogist*, 80, 549-559.
- 310 Batt, G.E., & Braun, J. (1999). The tectonic evolution of the Southern Alps, New Zealand: Insights
311 from fully thermally coupled dynamical modelling. *Geophysical Journal International*, 136, 403-
312 420.
- 313 Chivas, A.R. (1981). Geochemical evidence for magmatic fluids in porphyry copper mineralization.
314 Part I. Mafic silicates from the Koloula Igneous Complex. *Contribution to Mineralogy and*
315 *Petrology*, 78, 389-403.
- 316 Fujiwara, O., Sanga, T., & Ohmori, H. (1999). Regional distribution of erosion rates over the Japanese
317 Islands. *Japan Nuclear Cycle Technical Review*, 5, 85–93 (in Japanese with English abstract).
- 318 Hammarstrom, J.M., & Zen, E-an. (1986). Aluminum in hornblende: An empirical igneous
319 geobarometer. *American Mineralogist*, 71, 1297-1313.
- 320 Hartung, E., Caricchi, L., Floess, D., Wallis, S., Harayama, S., Kouzmanov, K., & Chiaradia, M. (2017).
321 Evidence for Residual Melt Extraction in the Takidani Pluton, Central Japan. *Journal of Petrology*,
322 58, 763–788.
- 323 Harayama, S. (2015). Vertically turned Quaternary collapsed caldera and Kurobegawa Granite
324 complex, exposed around the Mt. Kashimayari and Mt. Jii, Northern Japan Alps: *The Journal of*

- 325 the Geological Society of Japan, 121, 293–308 (in Japanese).
- 326 Harayama, S., Takahashi, M., Shukukawa, R., Itaya, T., & Yagi, K. (2010). High-temperature hot
327 springs and Quaternary Kurobegawa Granite along the Kurobegawa River. *Journal of Geological*
328 *Society of Japan*, 116, Supplement, 63–81 (in Japanese).
- 329 Holland, T., & Blundy, J. (1994). Non-ideal interactions in calcic amphiboles and their bearing on
330 amphibole-plagioclase thermometry. *Contributions to Mineralogy and Petrology*, 116, 433-447.
- 331 Imai, N., Terashima, S., Ohta, A., Mikoshihara, M., Okai, T., Tachibana, Y., Togashi, S., Matsuhisa, Y.,
332 Kanai, Y., Kamioka, H., & Taniguchi, M. (2004). *Geochemical map of Japan*. Geological Survey
333 of Japan, AIST, 209p.
- 334 Ito, H., Yamada, R., Tamura, A., Arai, S., Horie, K., & Hokada, T. (2013). Earth's youngest exposed
335 granite and its tectonic implications: the 10–0.8 Ma Kurobegawa Granite. *Scientific Reports*, 3,
336 1306, <https://doi.org/10.1038/srep01306>
- 337 Ito, H., Spencer, C.J., Danišik, M., & Hoiland, C.W. (2017). Magmatic tempo of Earth's youngest
338 exposed plutons as revealed by detrital zircon U-Pb geochronology. *Scientific Reports*, 7, 12457,
339 <https://doi.org/10.1038/s41598-017-12790-w>
- 340 Iwano H., Orihashi Y., Hirata T., Ogasawara, M., Danhara, T., Horie, K., Hasebe, N., Sueoka, S.,
341 Tamura, A., Hayasaka, Y., Katsube, A., Ito, H., Tani, K., Kimura, J.-I., Chang, Q., Kouchi, Y.,
342 Haruta, Y., & Yamamoto, K. (2013). An interlaboratory evaluation of OD-3 zircon for use as a

- 343 secondary U–Pb dating standard. *Island Arc* 22, 382–394.
- 344 Johannes, W., & Holtz, W. (1996). *Petrogenesis and Experimental Petrology of Granitic Rocks*.
345 Springer-Verlag, Berlin Heidelberg.
- 346 Ludwig, K., (2012). *User’s manual for Isoplot version 3.75–4.15: a geochronological toolkit for*
347 *Microsoft Excel*. Berkley Geochronological Center Special Publication 5.
- 348 Matsushi, Y., Matsuzaki, H., & Chigira, M. (2014). Determining long-term sediment yield from
349 mountainous watersheds by terrestrial cosmogenic nuclides. *Journal of the Japan Society of*
350 *Engineering Geology*, 54, 272-280. (in Japanese with English abstract)
- 351 Mutch, E.J.F., Blundy, J.D., Tattitch, B.C., Cooper, F.J., & Brooker, R.A. (2016). An experimental
352 study of amphibole stability in low-pressure granitic magmas and a revised Al-in-hornblende
353 geobarometer. *Contributions to Mineralogy and Petrology*, 171, 85.
354 <https://doi.org/10.1007/s00410-016-1298-9>
- 355 Ogata, S., Miyakoshi, K., Shidahara, T., & Tanaka, K. (1983). *Geology of the Kurobe geothermal area*.
356 *Central Research Institute of Electric Power Industry Report*, 382032, 27p. (in Japanese with
357 English abstract)
- 358 Ohmori, H. (1978). Relief structure of the Japanese mountains and their stages geomorphic
359 development. *Bulletin of the Department of Geography, University of Tokyo*, 10, 31-83.
- 360 Oikawa, T., & Wada, H. (2004). Rapid uplifting in the northern part of Hida Mountain Range at 1 Ma,

- 361 based on lithofacies and petrography in the Iyari Formation. *Journal of the Geological Society of*
362 *Japan*, 110, 528-535. (in Japanese with English abstract)
- 363 Reiners, P.W., & Brandon, M.T. (2006). Using thermochronology to understand orogenic erosion.
364 *Annual Review of Earth and Planetary Science*, 34, 419-466.
365 <https://doi.org/10.1146/annurev.earth.34.031405.125202>
- 366 Ring, U., Brandon, M.T., Willett, S.D., & Lister, G.S. (1999) Exhumation processes. *Geological*
367 *Society, London, Special Publications*, 154, 1-27.
- 368 Rioux, M., Bowring, S., Cheadle, M., & John, B. (2015). Evidence for initial excess ^{231}Pa in mid-
369 ocean ridge zircons. *Chemical Geology*, 397, 143–156.
- 370 Sakata, S., Hirakawa, S., Iwano, H., Danhara, T., Guillong, M., & Hirata, T. (2017). A new approach
371 for constraining the magnitude of initial disequilibrium in Quaternary zircons by coupled uranium
372 and thorium decay series dating, *Quaternary Geochronology*, 38, 1-12.
- 373 Sakata, S. (2018). A practical method for calculating the U-Pb age of Quaternary zircon: Correction
374 for common Pb and initial disequilibria. *Geochemical Journal*, 52, 281–286.
- 375 Schmitt, A.K. (2011). Uranium series accessory crystal dating of magmatic processes. *Annual Review*
376 *of Earth and Planetary Sciences*, 39, 321–349.
- 377 Schmidt, M.W. (1992). Amphibole composition in tonalite as a function of pressure: an experimental
378 calibration of the Al-in-hornblende barometer. *Contributions to Mineralogy and Petrology*, 110,

- 379 304-310.
- 380 Spencer, C.J., Danišik, M., Ito, H., Hoiland, C., Tapster, S., Jeon, H., McDonald, B., & Evans, N.J.
- 381 (2019). Rapid Exhumation of Earth's Youngest Exposed Granites Driven by Subduction of an
- 382 Oceanic Arc. *Geophysical Research Letters*, 46, 1259-1267.
- 383 Sueoka, S., & Tagami, T. (2019). Low-temperature thermochronology and its application to tectonics
- 384 in the shallow crust. *Journal of Geography (Chigaku Zasshi)*, 128, 707-730.
- 385 Wiedenbeck, M., Alle, P., Corfu, F., Griffin, W.L., Meier, M., Oberli, F., Vob Quadt, A., Roddick, J.C.,
- 386 & Spiegel, W. (1995). Three natural zircon standards for U–Th–Pb, Lu–Hf, trace element and
- 387 REE analyses. *Geostandards Newsletter*, 19, 1–23.
- 388 Wiedenbeck, M., Hanchar, J.M., Peck, W.H., Sylvester, P., Valley, J., et al. (2004). Further
- 389 characterisation of the 91500 zircon crystal. *Geostandards and Geoanalytical Research*, 28, 9–39.
- 390 Yamada, R. (1997). *Fission Track Thermochronology: Thermal Characteristics of Fission Tracks in*
- 391 *Zircon, and Cooling History Analysis of the Granitic Bodies around the Northern Alps, Central*
- 392 *Japan*. 128p. Kyoto University doctoral dissertation. <https://doi.org/10.11501/3123276>
- 393 Yamada, R., & Harayama, S. (1999). Fission track and K-Ar dating on some granitic rocks of the Hida
- 394 mountain range, Central Japan. *Geochemical Journal*, 33, 59-66.
- 395 Yamaguchi, Y., Wada, H., Ohta, Y., & Harayama, S. (2003). Amphibole zoning, a record of progressive
- 396 oxidation during crystallization of mafic microgranular enclaves in the Kurobegawa granitic

397 pluton. Journal of Mineralogical and Petrological Sciences, 98, 151-155.

398

399 **Figure captions**

400 Figure 1 Simplified geological map of the Kurobe area modified after [Harayama et al. \(2010\)](#) and
 401 [Harayama \(2015\)](#). Sample localities are also shown. The approximate emplacement ages (Ma) are
 402 indicated by the subscript numbers attached to F, G and V following [Harayama \(2015\)](#). MTL: Median
 403 Tectonic Line, ISTL: Itoigawa-Shizuoka Tectonic Line.

404

405 Figure 2 Photomicrographs, back scattered electron (BSE) image and X-ray elemental maps of an
 406 amphibole in sample KRG 16-07. (a) Photomicrograph of an amphibole-bearing domain. Plane
 407 polarized light (PPL). (b) Crossed polarized light (CPL) of (a). (c) BSE image of the same area as (a)
 408 and (b). White square represents the area for the X-ray elemental mapping shown in (d)-(k). (d)-(k)
 409 X-ray elemental maps for (d) Fe, (e) Al, (f) Mg, (g) Cl, (h) Na, (i) Ca, (j) Ti and (k) K. Note that albitic
 410 plagioclase and chloritized biotite are enclosed in Al-poor patchy replacements. Amp: amphibole, An:
 411 anorthite, Ap: apatite, Bt: biotite, Chl: chlorite, Ilm: ilmenite, Kfs: K-feldspar, Mag: magnetite, Pl:
 412 plagioclase, Qtz: quartz, Ttn: titanite.

413

414 Figure 3 Chemical composition of amphibole (O = 23) in sample KRG 16-07. (a) (Na+K) in A-site vs

415 Si, (b) Cl vs Al_{IV} , (c) $Mg/(Mg+Fe^{2+})$ vs Si, (d) $Mg/(Mg+Fe^{2+})$ vs Al_{IV} . Solid black lines represent
416 compositional boundaries of amphiboles. Blue broken lines represent Si = 7.3 a.p.f.u. and Al_{IV} = 0.7
417 a.p.f.u.

418

419 Figure 4 Photomicrographs, BSE image and X-ray elemental maps of an amphibole in sample KRG
420 16-101. (a) Photomicrograph of an amphibole-bearing domain. PPL. (b) CPL photo of (a). (c) BSE
421 image of the boxed area in (b). (d)-(k) X-ray elemental maps for the boxed area in terms of (d) Si, (e)
422 Fe, (f) Al, (g) Mg, (h) Cl, (i) Na, (j) Ca, (k) Ti and (l) K. Note that albitic plagioclase and chloritized
423 biotite are enclosed in Al-poor patchy replacements.

424

425 Figure 5 Chemical composition of amphibole (O = 23) in sample KRG 16-101. (a) (Na+K) in A-site
426 vs Si, (b) Cl vs Al_{IV} , (c) $Mg/(Mg+Fe^{2+})$ vs Si, (d) $Mg/(Mg+Fe^{2+})$ vs Al_{IV} . Solid black lines represent
427 compositional boundaries of amphiboles. Blue broken lines represent Si = 7.3 a.p.f.u. and Al_{IV} = 0.7
428 a.p.f.u.

429

430 Figure 6 (a) Conventional (Wetherill) and (b) Tera–Wasserburg concordia diagrams for U-Pb zircon
431 dating of KRG 16-101. Inset in (a) is an example of CL image of a dated zircon grain (spot KRG 16-
432 101-09).

433

434 Figure 7 *P-T* diagrams showing the estimated solidification conditions for (a) KRG 16-07 and (b)435 KRG 16-101. A water-saturated haplogranite solidus line is from [Johannes and Holtz \(1996\)](#).

436

437 Table S1 Instrumentation and operational settings for LA-ICP-MS analysis.

438

439 Table S2 (a) Results of LA-ICP-MS U-Pb zircon dating with common Pb correction assuming

440 initial equilibrium. (b) Results of LA-ICP-MS U-Pb zircon dating with common Pb correction

441 assuming initial disequilibrium.

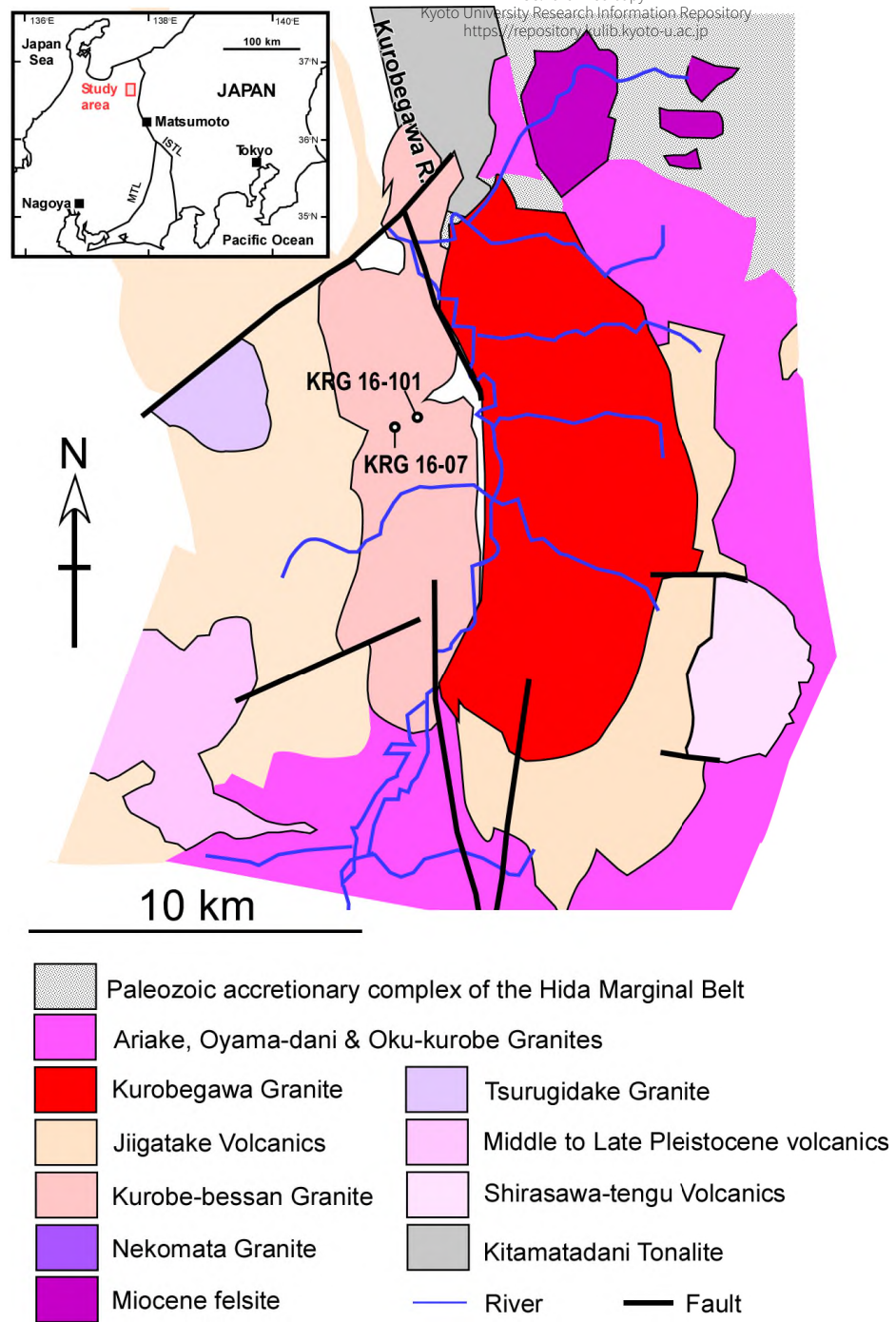


Fig. 1

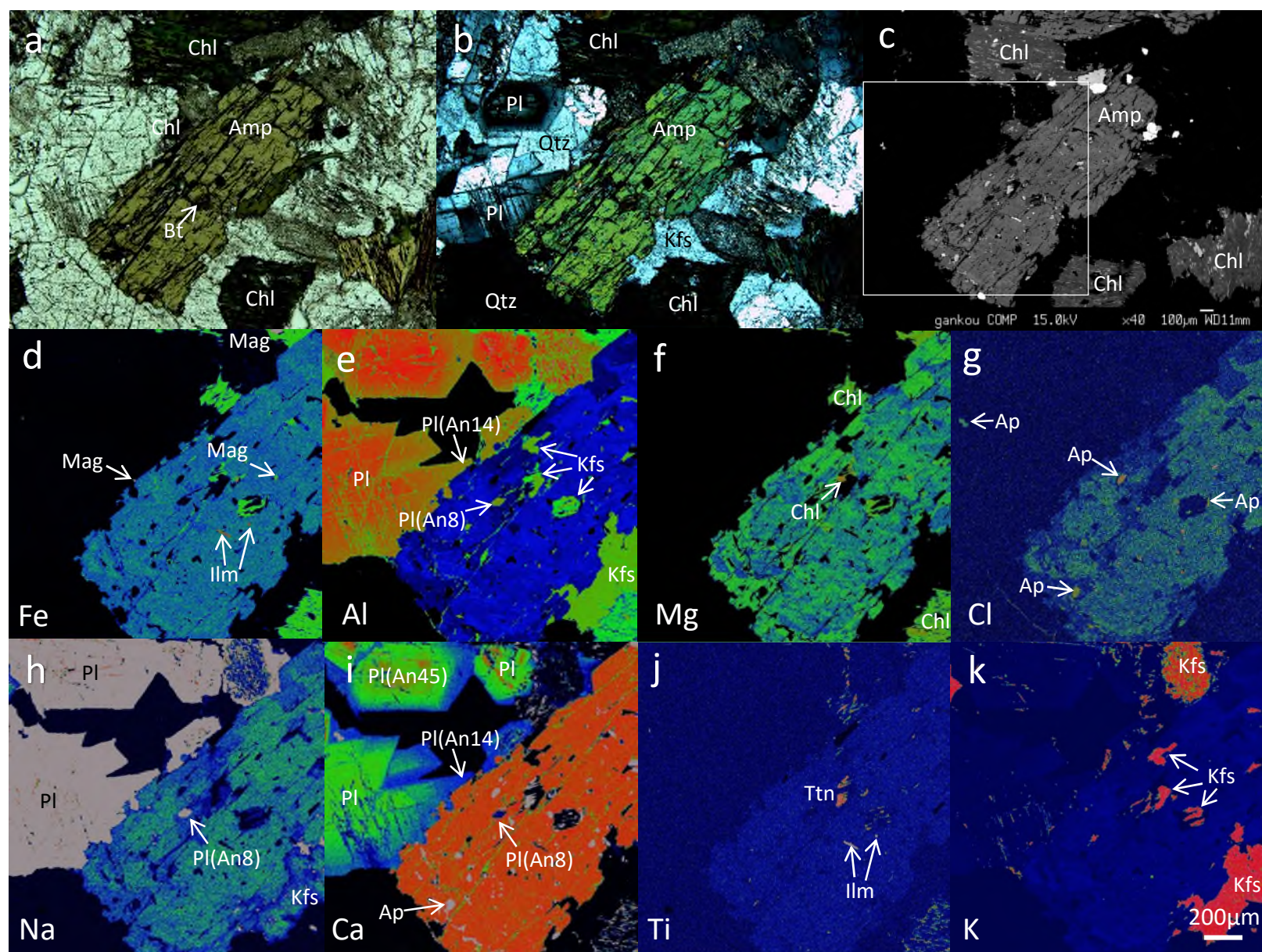


Fig. 2

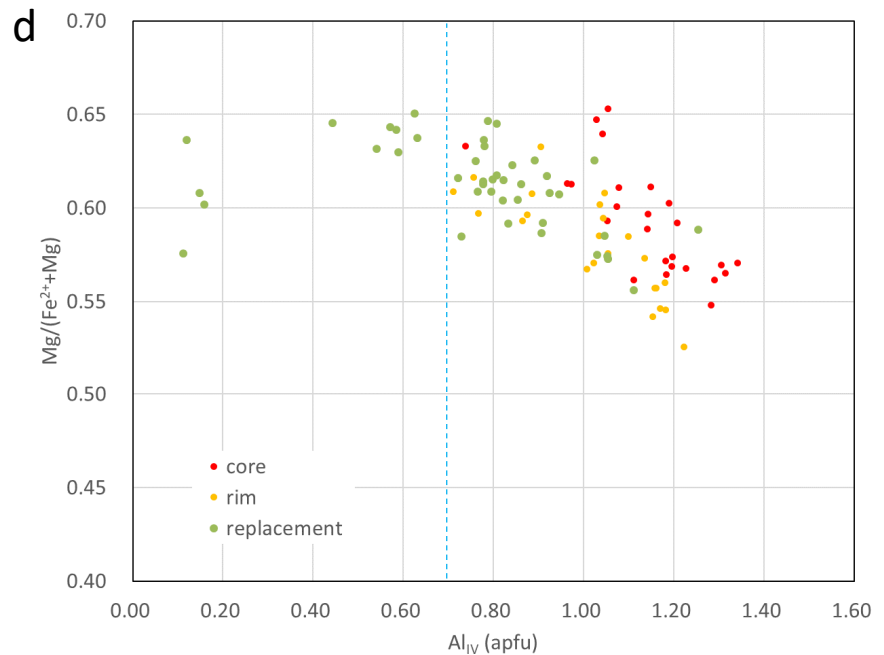
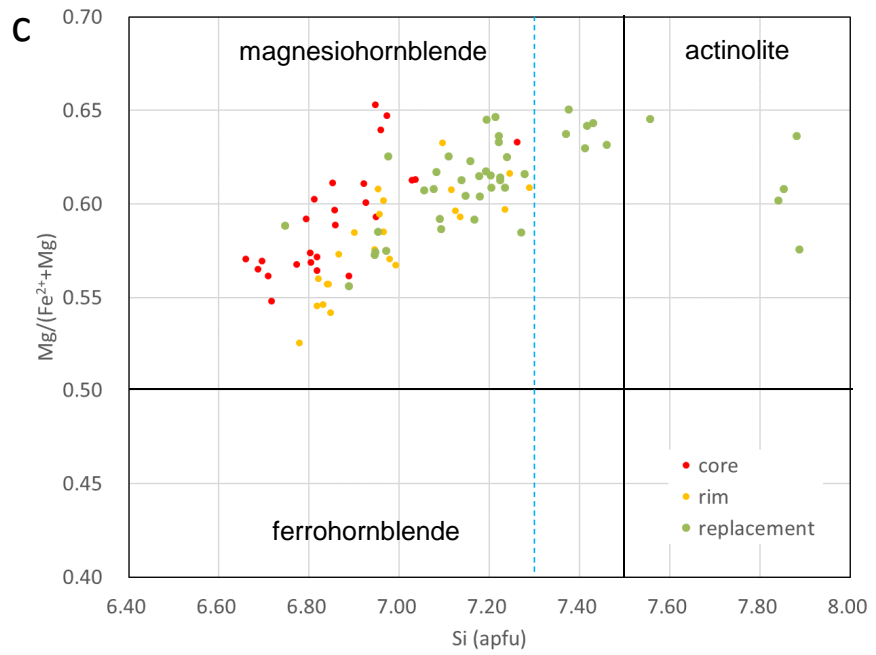
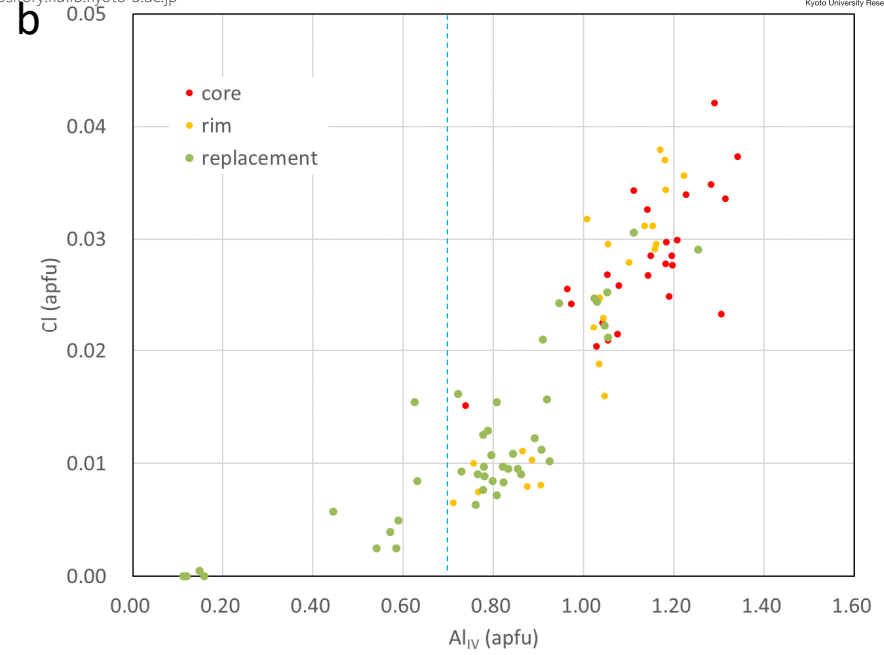
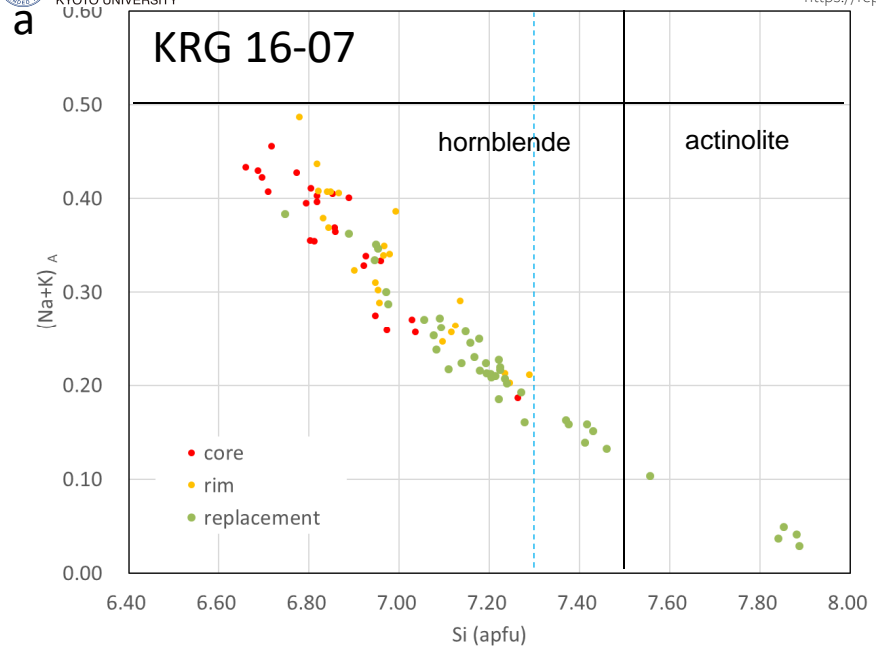


Fig. 3

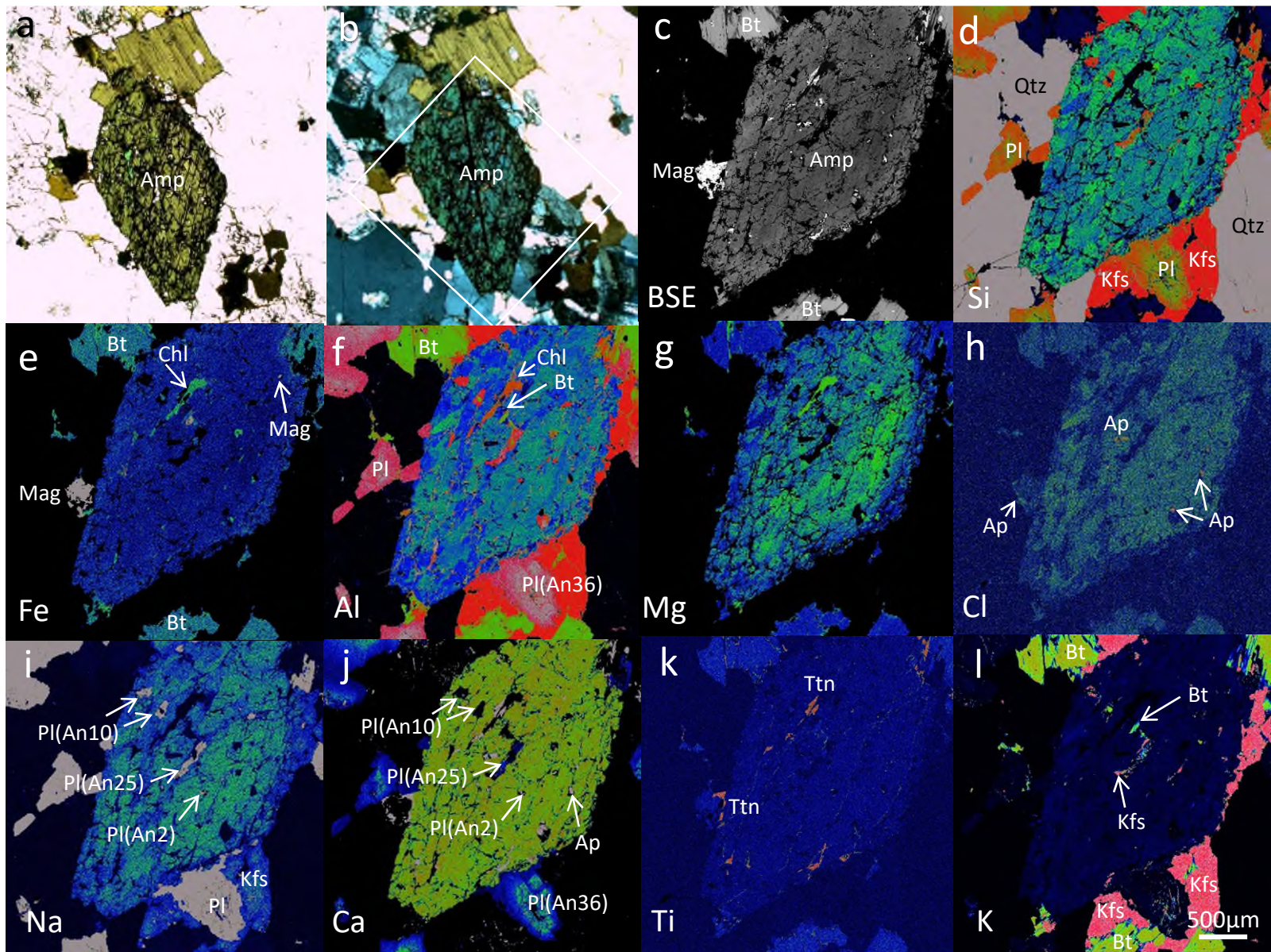


Fig. 4

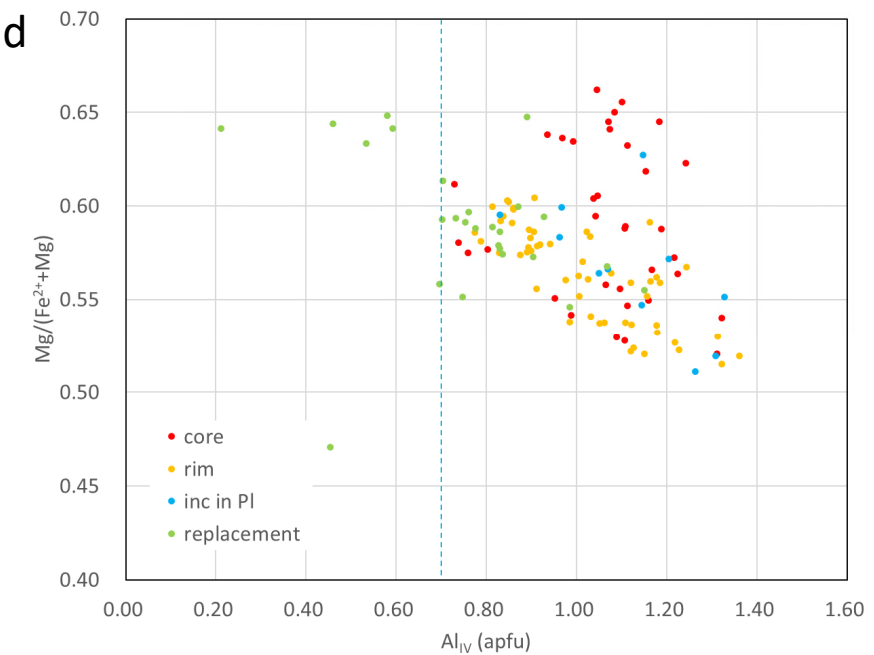
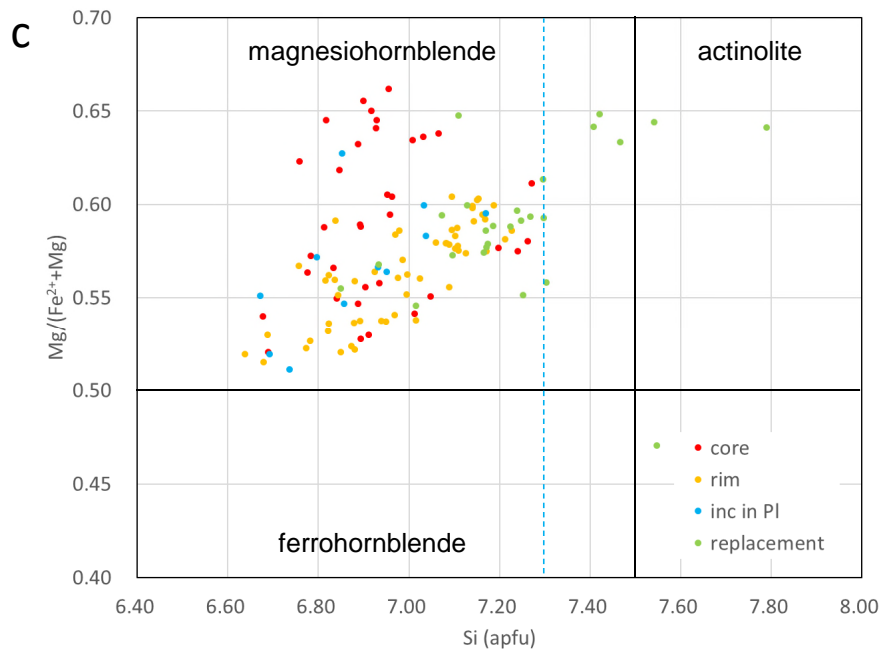
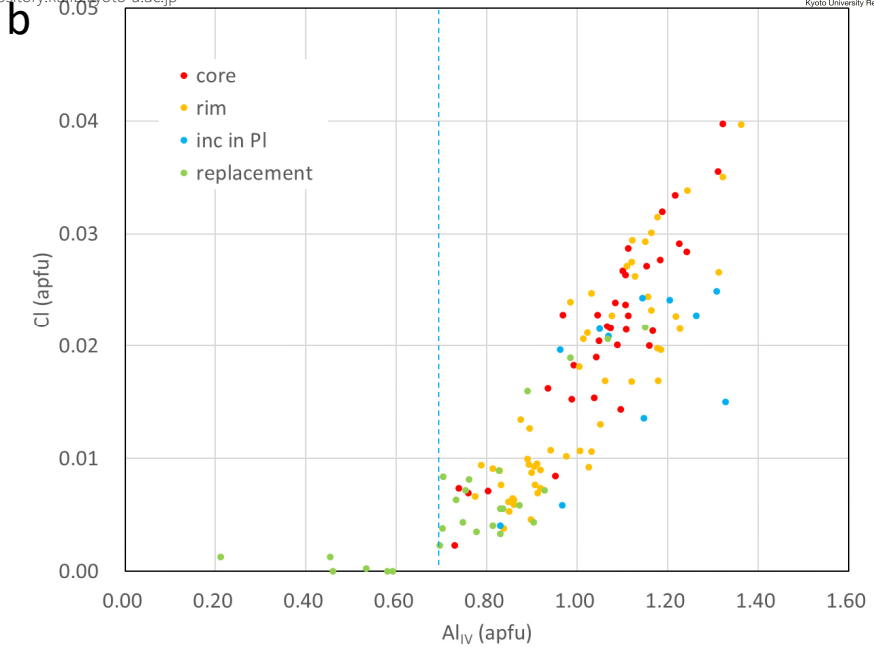
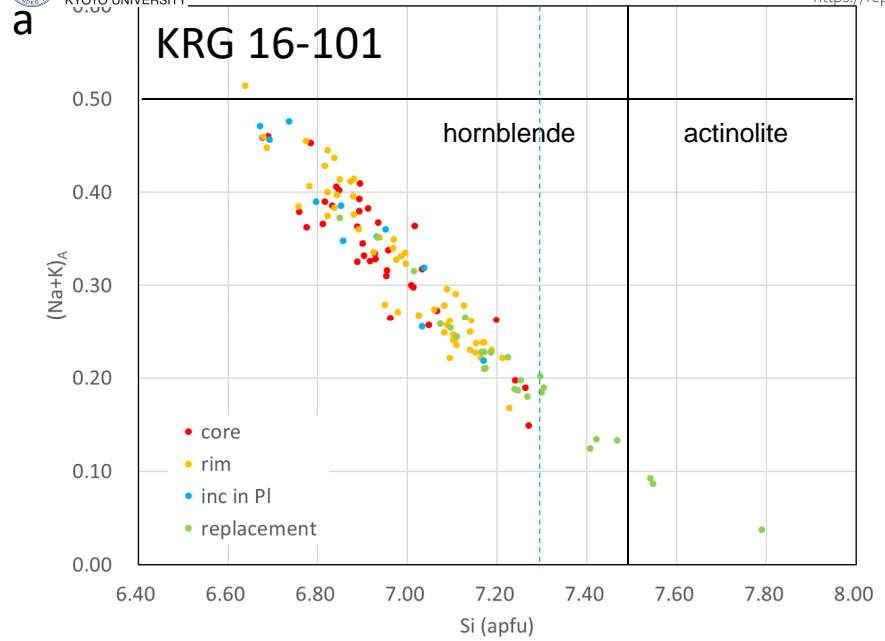


Fig. 5

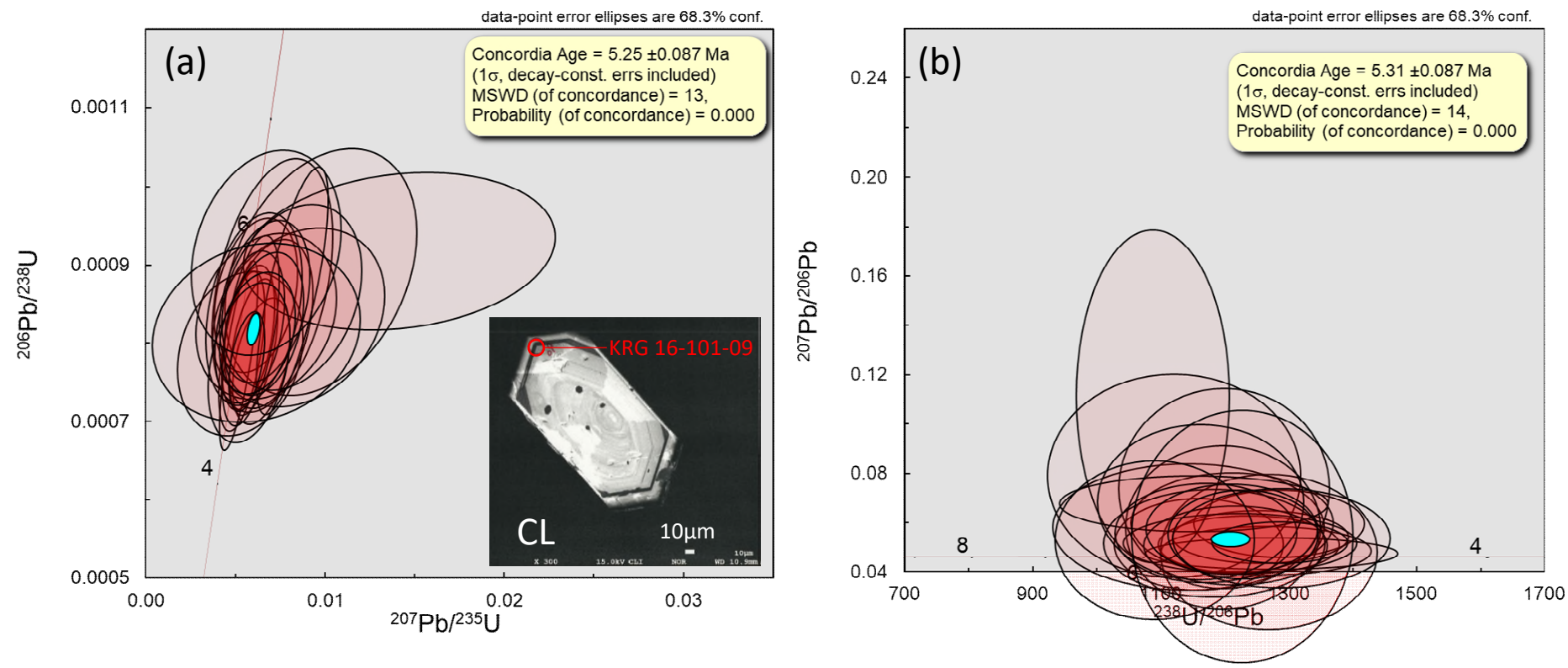


Fig. 6

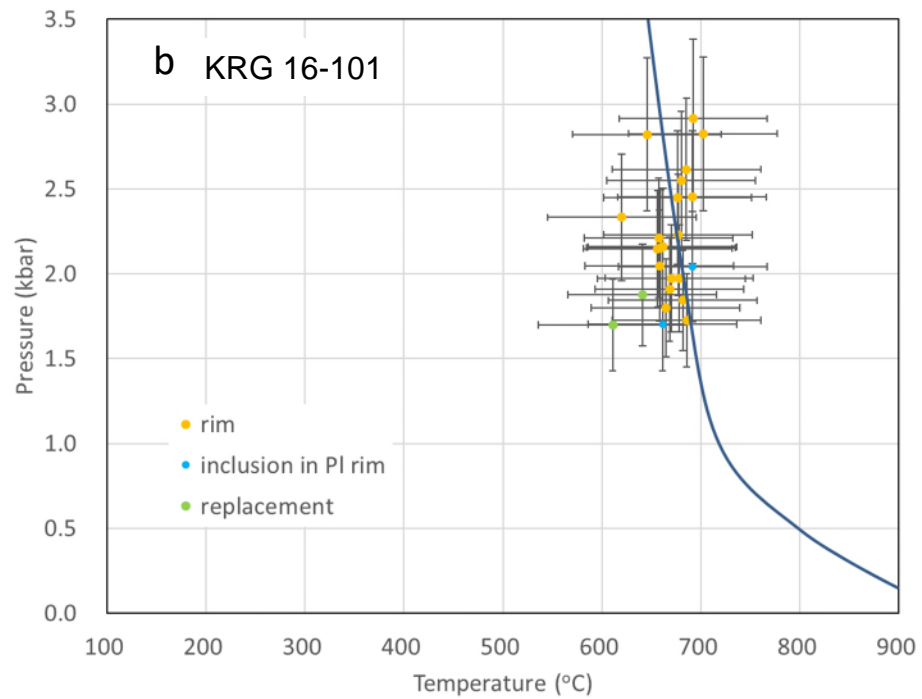
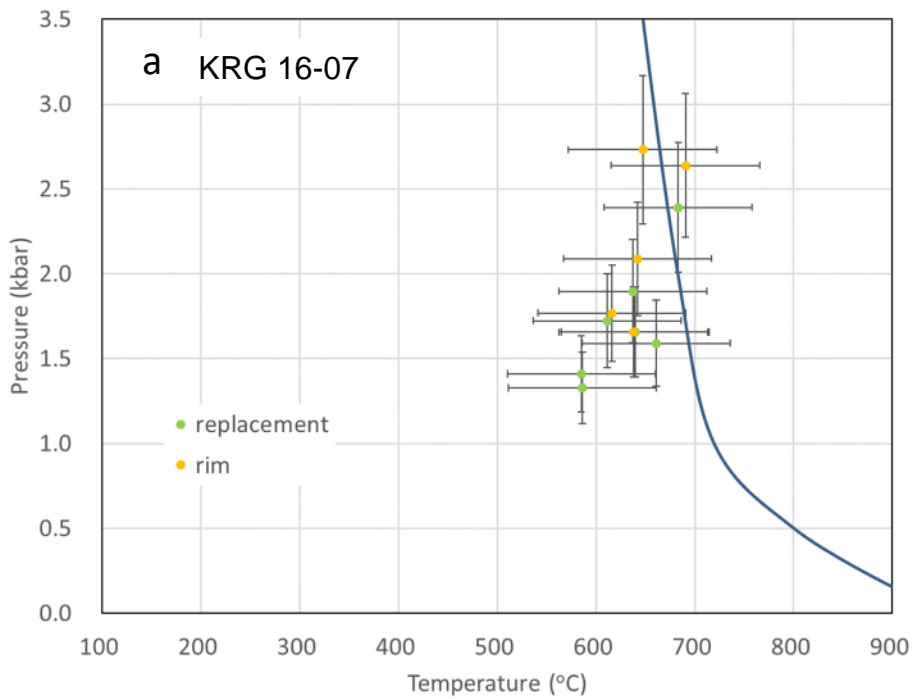


Fig. 7

Laboratory JAEA- Toki Geochronology Research Laboratory
Analyst S. Kagami, T. Yokoyama

Laser ablation system

Model Photon-Machines Analyte G2

Laser type Excimer 193 nm

Energy density 2.0 J cm⁻²

Crater size 20 μm circle

Repetition rate 10 Hz (200 shots)

Carrier gas He

He gas flow rate 1.0 L/min

ICP-MS

Model Thermo Fisher Scientific Neptune-*Plus*

Forward power 1200 W

Carrier gas Ar

Ar gas flow rate 1.1 L/min

Scanning mode Multi-collector Static

Data acquisition

protocol Time resolved analysis

Integration time 0.066s × 700 ratios

Monitor isotopes ²⁰²Hg (CDD), ²⁰⁴Pb (CDD), ²⁰⁶Pb (SEM), ²⁰⁷Pb (SEM),

²⁰⁸Pb (SEM), ²³²Th (FC), ²³⁸U (FC)

*CDD: Compact Discrete Dynode, SEM: Secondary Electron
Multiplier, FC: Faraday Cup

Primary standard 91500

Secondary standard OD-3

Table S2a. Results of LA – ICP – MS U – Pb zircon dating with common Pb correction assuming initial equilibrium.

analysis no.	microtexture	$^{207}\text{Pb}/^{235}\text{U}$	error (1 σ)	$^{206}\text{Pb}/^{238}\text{U}$	error (1 σ)	Error correlation	$^{207}\text{Pb}/^{206}\text{Pb}$	error (1 σ)	common $^{207}\text{Pb}/^{206}\text{Pb}$	error	f_{ThU}	error (30%)	f_{PaU}	error (30%)	Common Pb corrected age (Ma)	error (1 σ)	Th (ppm)	U (ppm)	Th/U	* excluded from weighted average
KRG16-101-1	unzoned mantle	8.40462	0.76642	0.07334	0.00608	0.90954	0.83109	0.03150	0.83594	0	1	0	1	0	456.3	36.6	n.d.	n.d.	n.d.	*
KRG16-101-2	oscillatory-zoned rim	0.00639	0.00106	0.00078	0.00005	0.41295	0.05964	0.00901	0.83594	0	1	0	1	0	4.9	0.3	629	739	0.85	
KRG16-101-3	oscillatory-zoned rim	0.00531	0.00085	0.00079	0.00007	0.53741	0.04874	0.00655	0.83594	0	1	0	1	0	5.1	0.4	600	893	0.67	
KRG16-101-4	oscillatory-zoned rim	0.00568	0.00096	0.00081	0.00006	0.44623	0.05104	0.00774	0.83594	0	1	0	1	0	5.2	0.4	391	674	0.58	
KRG16-101-5	unzoned mantle	0.00610	0.00153	0.00086	0.00006	0.29956	0.05130	0.01231	0.83594	0	1	0	1	0	5.5	0.4	269	379	0.71	
KRG16-101-6	oscillatory-zoned rim	0.02174	0.00997	0.00326	0.00146	0.97558	0.04835	0.00487	0.83594	0	1	0	1	0	20.9	6.5	n.d.	n.d.	n.d.	*
KRG16-101-7	unzoned mantle	0.00597	0.00089	0.00080	0.00006	0.48540	0.05444	0.00707	0.83594	0	1	0	1	0	5.1	0.3	1453	1132	1.28	
KRG16-101-8	unzoned mantle	25.41318	6.34566	0.21903	0.05350	0.97819	0.84149	0.04364	0.83594	0	1	0	1	0	1276.8	289.3	n.d.	n.d.	n.d.	*
KRG16-101-9	oscillatory-zoned rim	0.00515	0.00070	0.00078	0.00008	0.75091	0.04759	0.00427	0.83594	0	1	0	1	0	5.0	0.5	1064	1846	0.58	
KRG16-101-10	unzoned	9.41347	1.10182	0.08136	0.00890	0.93451	0.83913	0.03496	0.83594	0	1	0	1	0	504.2	53.3	n.d.	n.d.	n.d.	*
KRG16-101-11	oscillatory-zoned rim	0.00973	0.00353	0.00089	0.00010	0.32086	0.07917	0.02724	0.83594	0	1	0	1	0	5.5	0.6	404	949	0.43	
KRG16-101-12	oscillatory-zoned rim	0.00601	0.00177	0.00084	0.00008	0.32705	0.05166	0.01438	0.83594	0	1	0	1	0	5.4	0.5	169	327	0.52	
KRG16-101-13	oscillatory-zoned rim	0.00702	0.00222	0.00087	0.00011	0.38820	0.05825	0.01693	0.83594	0	1	0	1	0	5.5	0.6	221	343	0.64	
KRG16-101-14	oscillatory-zoned rim	0.00575	0.00129	0.00082	0.00006	0.34910	0.05082	0.01064	0.83594	0	1	0	1	0	5.3	0.4	317	541	0.59	
KRG16-101-15	oscillatory-zoned rim	0.00523	0.00230	0.00079	0.00007	0.20054	0.04816	0.02073	0.83594	0	1	0	1	0	5.1	0.4	203	221	0.92	
KRG16-101-16	oscillatory-zoned rim	0.00659	0.00165	0.00085	0.00007	0.31936	0.05597	0.01331	0.83594	0	1	0	1	0	5.4	0.4	296	426	0.69	
KRG16-101-17	oscillatory-zoned rim	0.00682	0.00164	0.00082	0.00007	0.35975	0.05997	0.01344	0.83594	0	1	0	1	0	5.2	0.4	321	420	0.76	
KRG16-101-18	oscillatory-zoned rim	0.00811	0.00257	0.00086	0.00008	0.28748	0.06846	0.02080	0.83594	0	1	0	1	0	5.4	0.5	204	256	0.80	
KRG16-101-19	oscillatory-zoned rim, crack	0.00849	0.00317	0.00083	0.00008	0.24292	0.07388	0.02676	0.83594	0	1	0	1	0	5.2	0.5	206	190	1.08	*
KRG16-101-20	oscillatory-zoned rim, crack	0.00654	0.00146	0.00083	0.00006	0.32817	0.05749	0.01211	0.83594	0	1	0	1	0	5.2	0.4	341	461	0.74	*
KRG16-101-21	oscillatory-zoned rim	0.00668	0.00259	0.00083	0.00007	0.21654	0.05806	0.02196	0.83594	0	1	0	1	0	5.3	0.4	116	224	0.52	
KRG16-101-22	oscillatory-zoned rim	0.00558	0.00066	0.00078	0.00004	0.45816	0.05208	0.00550	0.83594	0	1	0	1	0	5.0	0.3	879	1840	0.48	
KRG16-101-23	unzoned rim	0.01410	0.00574	0.00092	0.00007	0.17825	0.11140	0.04459	0.83594	0	1	0	1	0	5.4	0.5	124	254	0.49	
KRG16-101-24	oscillatory-zoned rim	0.00573	0.00151	0.00078	0.00007	0.33107	0.05362	0.01333	0.83594	0	1	0	1	0	4.9	0.4	275	477	0.58	
KRG16-101-25	unzoned	4.92068	0.77426	0.04267	0.00642	0.95639	0.83631	0.03844	0.83594	0	1	0	1	0	269.4	39.8	n.d.	n.d.	n.d.	*
KRG16-101-26	unzoned	8.65497	1.09942	0.07489	0.00879	0.92402	0.83815	0.04071	0.83594	0	1	0	1	0	465.6	52.9	n.d.	n.d.	n.d.	*
KRG16-101-27	unzoned	7.94481	1.06792	0.06892	0.00861	0.92955	0.83603	0.04143	0.83594	0	1	0	1	0	429.7	52.2	n.d.	n.d.	n.d.	*
KRG16-101-28	unzoned	8.76559	1.69260	0.07486	0.01396	0.96585	0.84928	0.04249	0.83594	0	1	0	1	0	465.3	84.3	n.d.	n.d.	n.d.	*
KRG16-101-29	oscillatory-zoned rim	0.00812	0.00132	0.00087	0.00010	0.73813	0.06786	0.00746	0.83594	0	1	0	1	0	5.4	0.6	596	1076	0.55	
KRG16-101-30	oscillatory-zoned rim	0.00669	0.00276	0.00092	0.00009	0.22815	0.05299	0.02129	0.83594	0	1	0	1	0	5.9	0.5	114	195	0.58	
KRG16-101-31	oscillatory-zoned rim	0.03772	0.01384	0.00105	0.00013	0.33810	0.26046	0.08995	0.83594	0	1	0	1	0	4.9	0.9	555	565	0.98	
KRG16-101-32	oscillatory-zoned rim	0.00620	0.00139	0.00081	0.00005	0.28156	0.05527	0.01186	0.83594	0	1	0	1	0	5.2	0.3	340	566	0.60	
KRG16-101-33	unzoned	6.85524	0.64235	0.05887	0.00498	0.90367	0.84459	0.03389	0.83594	0	1	0	1	0	368.7	30.4	n.d.	n.d.	n.d.	*
KRG16-101-34	unzoned, crack	9.95498	1.52518	0.08506	0.01234	0.94689	0.84878	0.04181	0.83594	0	1	0	1	0	526.3	73.7	n.d.	n.d.	n.d.	*
KRG16-101-35	oscillatory-zoned rim	0.00581	0.00106	0.00082	0.00008	0.53712	0.05157	0.00797	0.83594	0	1	0	1	0	5.2	0.5	569	896	0.63	
KRG16-101-36	oscillatory-zoned rim	0.00613	0.00383	0.00081	0.00008	0.14815	0.05458	0.03377	0.83594	0	1	0	1	0	5.2	0.5	82	147	0.56	

n.d.: not determined

